ORIGINAL RESEARCH ARTICLE

Microstructure and Tribological Properties of FeCrBSi Amorphous Alloy Coatings by Ultra-High-Speed Laser Cladding

Feihuan Chen, Zhaobing Cai, Gang Liu, Xuming Pang, Le Gu, and Jibin Pu

In this paper, the microstructure and tribological properties of ultra-high-speed laser cladded FeCrBSi amorphous alloy coatings were investigated, focusing on the effects of laser power on the evolution of the coatings' microstructure, microhardness, and tribological properties. The results showed that the FeCrBSi amorphous alloy coating was mainly composed of amorphous phase, α-Fe, and intermetallic compounds of Fe with B and Si. With the increase of laser power, the amorphous phase decreased and the grain size became larger. The microhardness showed a trend of decreasing and then increasing, and the microhardness reached the maximum when the laser power was 2800W, which was related to the synergistic strengthening effect of amorphous, intermetallic compounds and nanocrystals within the coating. Also, the wear resistance of the coating was found to be the best when the laser power was 2800W, and the main wear mechanism of this coating was oxidative wear with major Fe-oxides and Si-oxides. Moreover, the trace Cr_2O_3 generated in the oxide layer could play a certain supporting lubrication role, leading to a decrease in wear rate.

Graphical Abstract
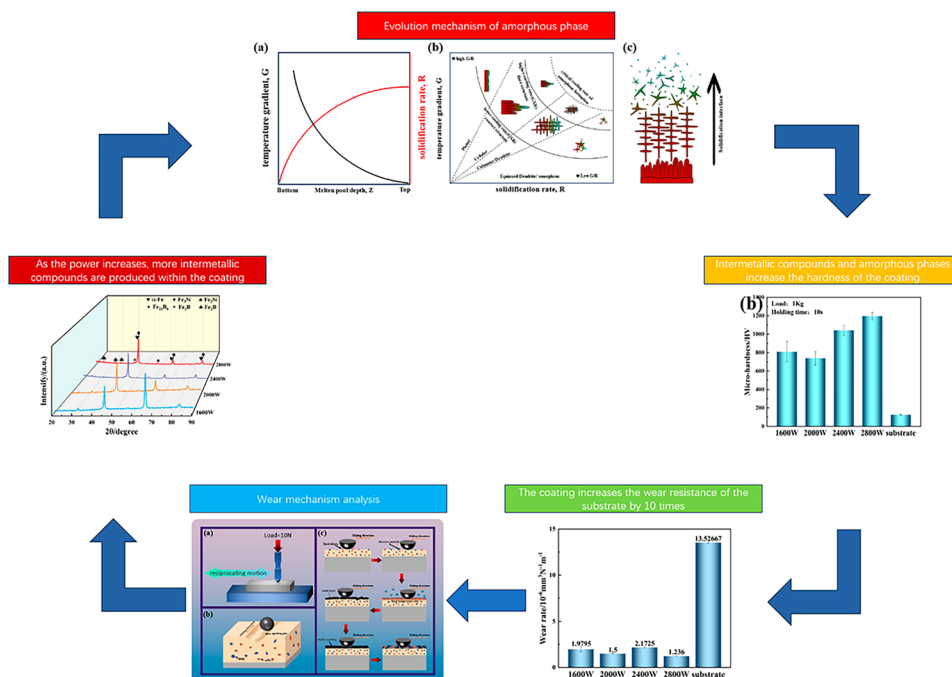
Feihuan Chen, Key Laboratory of Metallurgical Equipment and Control Technology, Ministry of Education, Wuhan University of Science and Technology, Wuhan 430081, China; and Key Laboratory of Marine Materials and Related Technologies, Key Laboratory of Marine Materials and Protective Technologies of Zhejiang Province, Ningbo Institute of Materials Technology and Engineering, Chinese Academy of Sciences, Ningbo 315201, China; **Zhaobing Cai** and **Le Gu**, Key Laboratory of Metallurgical Equipment and Control Technology, Ministry of Education, Wuhan University of Science and Technology, Wuhan 430081, China; and **Gang Liu, Xuming Pang,** and **Jibin Pu**, Key Laboratory of Marine Materials and Related Technologies, Key Laboratory of Marine Materials and Protective Technologies of Zhejiang Province, Ningbo Institute of Materials Technology and Engineering, Chinese Academy of Sciences, Ningbo 315201, China. Contact e-mail: caizhaobing@wust.edu.cn.

1. Introduction

In recent years, amorphous materials have attracted much attention because of their excellent mechanical properties such as high strength and hardness. There are many kinds of amorphous materials, such as Fe- (Ref 1), Co- (Ref 2), Al- (Ref 3), Ni- (Ref 4), Pd- (Ref 5), Zr- (Ref 6) and Cu- (Ref 7) based amorphous alloy. Among them, Fe-based amorphous materials exhibit excellent soft magnetic properties (Ref 8), considerable mechanical properties (Ref 9), better thermal stability, and relatively low price (Ref 10, 11), which are of more industrial importance in practical applications, due to the unique long-range disordered and short-range ordered sub-stable structure. However, the lack of glass formation capability limits the engineering applications of Fe-based amorphous alloys. Also, the extremely high cooling rate ($\sim 10^5$ K/s) of many Fe-based amorphous alloys limits their shapes and preparation (Ref 8, 12-15), therefore, improving the glass formation ability of Fe-based amorphous alloys is of great significance to drive their industrial applications.

Surface coating technology is a reliable method to expand its engineering applications by depositing a thin layer on the surface of the substrate to fulfill the function of Fe-based amorphous alloys while reducing the material cost. Nowadays, there are many surface coating technologies, including electroplating (Ref 16), thermal spraying (Ref 17), PVD, surface carburizing, surface nitriding, and laser cladding. Among these technologies, laser cladding has good amorphous formation performance due to its fast cooling rate and so on, and is currently the main technical means to prepare amorphous coatings. For example, Wuyan Yuan et al (Ref 18) prepared CNTs/FeCoNbBSi amorphous composite coating by laser cladding technique, which improved the wear and corrosion resistance of the coating as the amount of nickel-plated carbon nanotubes increased. Keyao Li et al (Ref 19) investigated the

effect of chromium content on the glass transition properties and mechanical properties of Fe-based amorphous composite coatings and found that an appropriate proportion of chromium content can effectively improve the glass transition properties and mechanical properties of Fe-based amorphous composite coatings. However, due to the high input energy density, and high dilution rate, the coating prepared by conventional laser melting has a low content of amorphous phase. Mingying Xiao et al. proposed a new process for ultra-high speed laser cladding of iron-based amorphous alloy coating. The experimental results show that with the increase in scanning speed, the amorphous content increases and the dilution rate decreases (Ref 20). Compared with conventional laser cladding shown in Fig. 1, ultra-high-speed laser cladding has low input energy density, high cooling rate, and low release rate, which can solve the above problems.

Although it is not a new discovery, there are very few relevant studies. Therefore, in this study, an attempt was made to prepare a Fe-based (FeCrBSi) amorphous alloy coating with increased hardness and wear resistance on medium carbon steel by ultra-high-speed laser cladding technology. The effects of laser power parameters on the microstructure, amorphous phase content, microhardness, and wear resistance of the coatings were investigated and discussed. The subsequent authors will conduct more in-depth research in the future on the basis of the data in this paper.

2. Experimental Details

2.1 Preparation of Fe-Based Amorphous Alloy Coating by Ultra-High-Speed Laser Cladding

The cladding powder used in the experiment was FeCrBSi amorphous alloy powder, and the composition of the powder is shown in Table 1. According to a large number of literature investigations, it is found that this iron-based amorphous alloy system has not appeared in the research related to laser cladding, but has only been used in thermal spraying. Therefore, this system is adopted to conduct the research related to laser cladding. The SEM morphology and XRD pattern of the Fe-based amorphous alloy powder are shown in Fig. 2, showing that
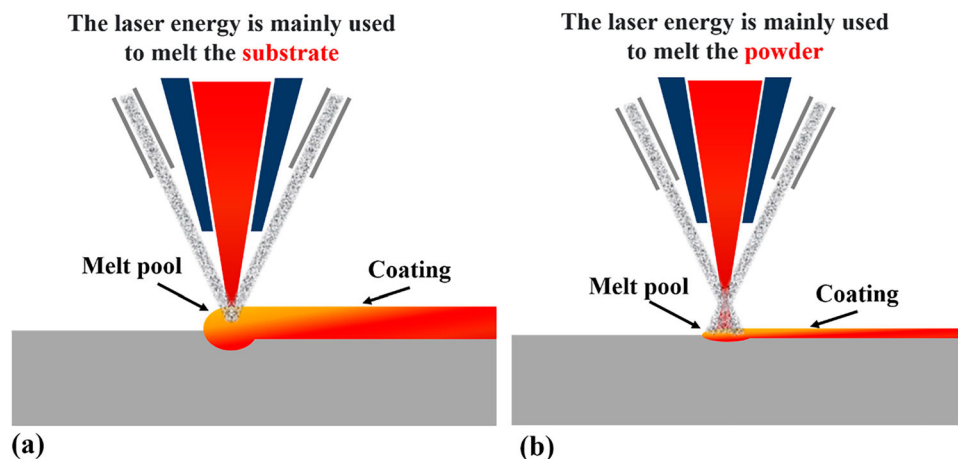
Fig. 1 Schematic illustration of (a) Traditional laser cladding and, (b) Ultra-high-speed laser cladding

the powder is spherical, with a size range of 10– 50 μm. In addition, in Fig. 2(b), there is a significantly wider diffuse scattering peak at 45°, indicating that the powder used has a high amorphous content. A 120 mm × 200 mm × 10 mm No. 45 steel pipe was selected as the cladding substrate. Before cladding, the surface of the substrate was sanded and polished, ultrasonically cleaned in acetone solution for 10 min, and then dried naturally. The Fe-based amorphous alloy coatings were prepared using an EHLA-Compact (C-ECS- 500/10) type ultra-high-speed laser cladding equipment with a maximum power of 4000W. The laser power was used as a variable in the experiment, and the process parameters were shown in Table 2, in which argon was used as a protective gas and a powder carrier gas. The energy input density E_S (J/mm^2) during the fusion coating process can be calculated according to Eq. 1 (Ref 21). The sample was cut into 10 mm × 10 mm × 10 mm sizes with a high-pressure water knife, and the cut sample was ultrasonically cleaned in acetone solution for 15 min.

$$E_s = P/(v \times d) \tag{Eq 1}$$

Table 1 Chemical composition of Fe-based amorphous alloy powder

| Element	Fe	Cr	B	Si
Wt.%	Bal.	2-3	2-3	5.5-7.5

P is the laser power W, v is the scanning rate mm/s, and d is the laser spot diameter mm.

2.2 Microstructure and Properties of Fe-Based Amorphous Alloy Coatings

A set of 10 mm × 10 mm × 10 mm samples were polished and a metallographic test was carried out after aqua regia corrosion. The microstructure of the coatings was observed using a FEI Quanta FEG 250 field emission scanning electron microscope equipped with an energy dispersive spectrometer. The other group of 10 mm × 10 mm × 10 mm samples was slightly polished on one side of the cladding coating, and the surface oxide film was polished until the metallic luster was exposed. The physical phase composition of the coatings was analyzed using an x-ray diffractometer (XRD) model D8 ADVANCE. The x-ray light source was a Cu target with a 2θ angle ranging from 20° to 90° and a scanning speed of 5°/min. The content of amorphous phases as a percentage of AP% can be estimated using a background method according to Eq. 2 (Ref 22).

$$AP\% = \frac{\text{integral area of the background}}{\text{integral area of original diffraction}} \tag{Eq 2}$$

HV-1000A micro Vickers hardness tester was used to measure the surface hardness of Fe-based amorphous alloy coating. In order to reduce the experimental error, 5 points were randomly selected on the surface of the coating. The test
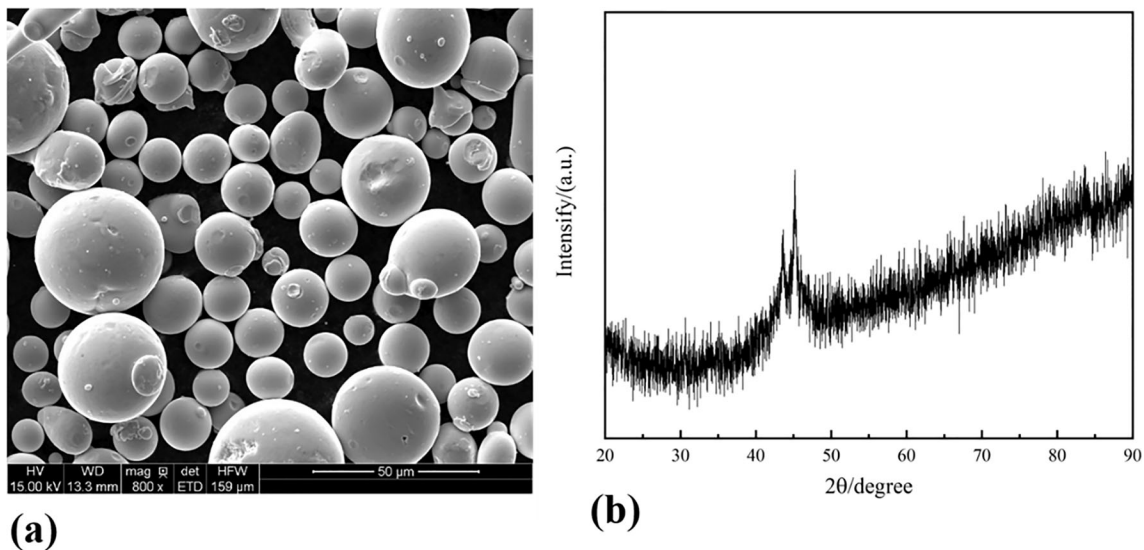
Fig. 2 Fe-based amorphous alloy powder for ultra-high-speed laser cladding: (a) SEM morphology and, (b) XRD pattern

Table 2 Parameters of ultra-high-speed laser cladding

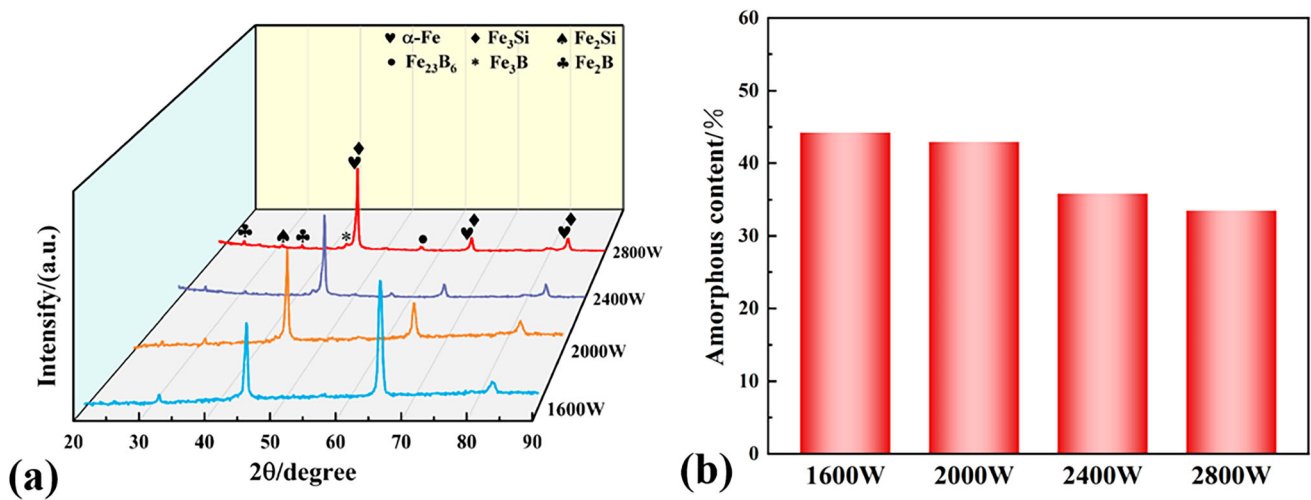| Power, W	Scanning speed, m/min	Powder feed rate, g/min	Protective gas flow, L/min	Spot diameter, mm	Defocusing amount, mm
1600	20	20	15	2	11
2000	20	20	15	2	11
2400	20	20	15	2	11
2800	20	20	15	2	11

Fig. 3 XRD patterns and amorphous content of coating at different laser power
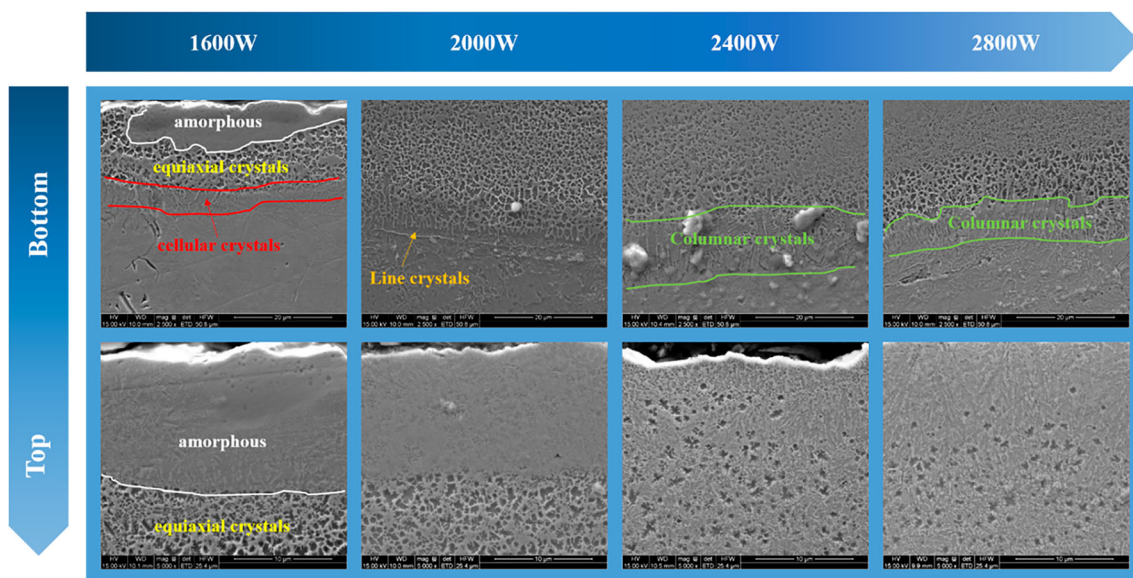

Fig. 4 Microstructure of ultra-high-speed laser cladding coating.

process parameters were as follows: loading 1 Kg, loading time 10 s.

UMT-3 friction and wear testing machine was used for axial sliding of the coating, and a 6 mm Si_3N_4 ball was used as the grinding ball. The loading load was 10N, the single sliding length was 5 mm, the sliding speed was 50 mm/s, and the friction time was 60 min. After the friction wear experiment, the abrasion contour was scanned using a UP-Lambda type 3D optical profiler to get the cross-sectional area of the abrasion contour, and the scanning was repeated three times to get the average value to reduce the experimental error. The coating wear rate R_W ($10^{-6} m^3 N^{-1} m^{-1}$) can be calculated according to Eq. 3 E. Rabinowitz equation (Ref 23).

$$R_w = V_w / (S \times N) \tag{Eq 3}$$

V_W is the wear volume m^3, S is the sliding distance m, and N is the load N.

3. Results and Discussion

Fig. 3 shows the XRD patterns of the coatings at different laser powers, from which it can be seen that the diffraction peaks around 45° show a diffuse broadening phenomenon, indicating that the coatings are composed of both amorphous and crystalline phases (Ref 24). The amorphous/ nanocrystalline phase ground composition has been reported in other studies (Ref 25). In addition, the coating was analyzed to contain α-Fe, Fe_3Si, Fe_2Si, $Fe_{23}B_6$, Fe_3B, and Fe_2B (Ref 24, 26, 27). It was observed that the intensity of the diffraction peaks of the 45° crystalline phase increased with increasing power, and $Fe_{23}B_6$, Fe_3B, and Fe_2B occurred in the coatings of 2400 W and 2800W. This is because as the power increases, the heat input becomes larger, and the solidification rate of the melt pool decreases, thus B combines more readily with Fe to form compounds. The amorphous phase content in the coating was calculated from Eq. 2 (Ref 22), as shown in Fig 3(b). The amorphous phase content in each coating was 44.21%
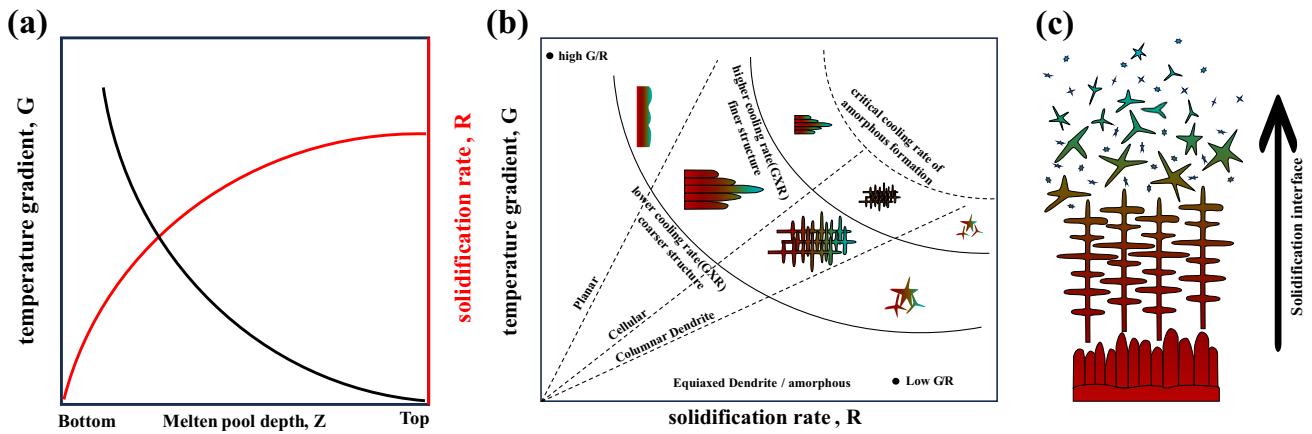
Fig. 5 (a) The relationship between temperature gradient (G) and solidification rate (R) concerning the depth of the molten pool (Ref 26); (b) The influence of temperature gradient (G) and solidification rate (R) on grain growth tendency; (c) Grain growth model in Fe-based amorphous coatings (Ref 25).
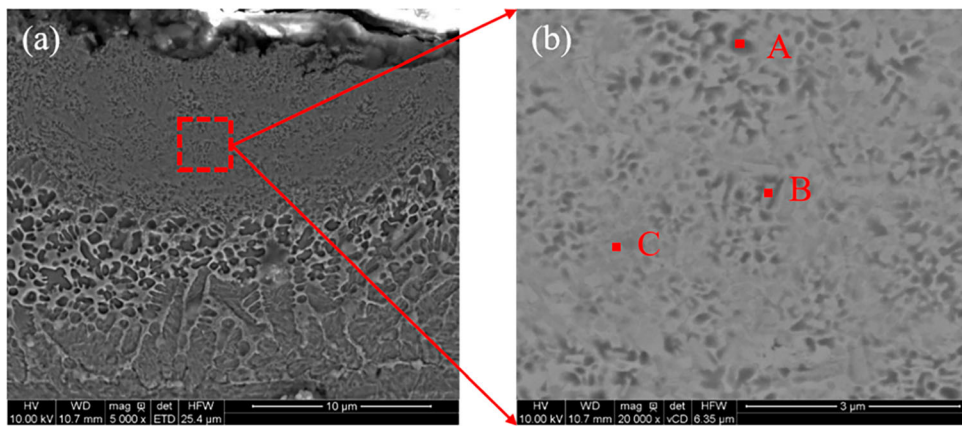
Fig. 6 SEM morphology of coating with laser power of 2800W: (a) Microtopography of the top of the coating, (b) Partial enlargement of the top of the coating

(1600W), 42.9% (2000W), 35.83% (2400W), and 33.47% (2800W), respectively. According to the literature investigation, the amorphous phase content in the coating of the iron-based amorphous alloy is generally low due to the concentrated heat input of laser cladding. As the power increased, the heat input energy density increased. The solidification rate R of the melt pool decreased, and the amorphous powder was more easily crystallized when it entered the melt pool. Therefore the higher the laser power, the less amorphous content in the coating.

Fig. 4 shows the microscopic morphology of the coating cross-section under different laser power, as shown in the figure, there is a good metallurgical bond between the coating and the substrate. The substrate and coating bonding area can be categorized into four typical morphologies: very thin planar crystals at the fusion and line, cellular crystals, columnar crystals, and equiaxial crystals. The top of the 1600W and 2000W coatings is an amorphous structure with no obvious characteristics, which is consistent with the results obtained by other researchers (Ref 24), and the tops of the 2400W and 2800W coatings showed equiaxed crystals, which were uniformly mixed with the amorphous phase. As the power increased, both the coating interface region and the top microstructure changed, which can be explained by the theory of rapid solidification (shown in Fig. 5).

Table 3 Elements composition of each point in Fig. 6(b) of Fe-based amorphous coating at 2800W

	Fe	Cr	Si	B
A	79.03	2.97	18.00	0
B	71.91	3.50	7.40	17.18
C	82.75	2.85	12.43	1.97

The coating mainly consists of coarse equiaxial crystals at the interface between the coating and substrate when exposed to a laser power of 1600W. This was due to the small temperature gradient (G) and high solidification rate (R) at the solid-liquid interface of the low-power melt pool, resulting in a small G/R ratio. At this time the grains in the formation and growth process began to grow in all directions, resulting in the formation of equiaxed crystals. With the solidification interface rising, the top of the melt pool was solidified before nucleation because the solidification rate R exceeded the critical cooling rate of amorphous formation. So the bottom of the 1600W coating was equiaxed and the top was amorphous. When the laser power was 2000W, G became larger and R decreased at

the bottom of the melt pool, resulting in a larger G/R. Cellular and planar crystals appeared at the bottom of the melt pool, and the cellular crystals grew along the cooling direction perpendicular to the substrate interface. However, the R at the top of the melt pool was still larger than the critical cooling rate of amorphous formation, so the bottom of the 2000W coating was planar crystal and cellular crystal, and the top was amorphous. At laser power of 2400W and 2800W, the heat input energy became large, G became extremely large, and R became extremely small, resulting in extremely high G/R. Planar crystals appeared at the bottom of the melt pool, and as the solidification interface rose, G decreased and R increased. The planar crystals began to transform into cellular crystals, while new grains continued to form and grow, and the grains preferentially grew along the cooling direction perpendicular to the basal interface, forming columnar dendrites. The R at the top of the melt pool was less than the critical cooling rate of

amorphous formation, and equiaxed crystals were generated, which were uniformly mixed with the amorphous.

Fig. 6(a) shows the microscopic morphology of the top of the Fe-based amorphous coating at 2800W, from which it can be seen that the morphology of the top of the coating distinguishes between crystalline and amorphous with, needle-like or columnar precipitates. Fig. 6(b) shows an enlarged view of the coating and it can be seen that there are three different contrast phases, that is, black, white, and gray. The black and gray phases are very small in size, both below 400 nm. The EDS points were analyzed for the areas labeled in Fig. 6(b), respectively, and the results are shown in Table. It can be seen from Table 3 that the black phase is the enrichment of the Si element, which is speculated to be Fe_3Si and Fe_2Si compounds. The grey phase is the enrichment of the B element, which is speculated to be $Fe_{23}B_6$, Fe_3B, and Fe_2B compounds. The element composition of the white phase is similar to that of the original powder, so it is presumed to be amorphous. So based on the above analysis, one conclusion can be confirmed that the top area of the coating was a mixture of amorphous and iron intermetallic compounds (IMC).

The average microhardness of the Fe-based amorphous alloy coatings is 809.057HV (1600W), 739.733HV (2000W), 1041.842 HV (2400W), and 1196.238 HV (2800W), respectively. As shown in Fig. 7, the coating microhardness varies considerably with power, and the microhardness is significantly higher than the substrate microhardness hardness ($\sim$120HV). The microhardness of the coatings tends to decrease and then increase as the laser power increases. The microhardness of the 2000W coating is lower than that of the 1600W coating because the amorphous phase content of the 2000W coating is lower than that of the 1600W coating, and the amorphous phase helps to improve the microhardness of the coating The microhardness of the 2400W and 2800W coatings was higher than that of the 1600W and 2000W coatings. Combined with the XRD patterns, the 2400W and 2800W coatings generated more types of intermetallic compounds. Intermetallic compounds are hard phases. The increase of laser power leads to the decrease of amorphous phase content and the increase of intermetallic
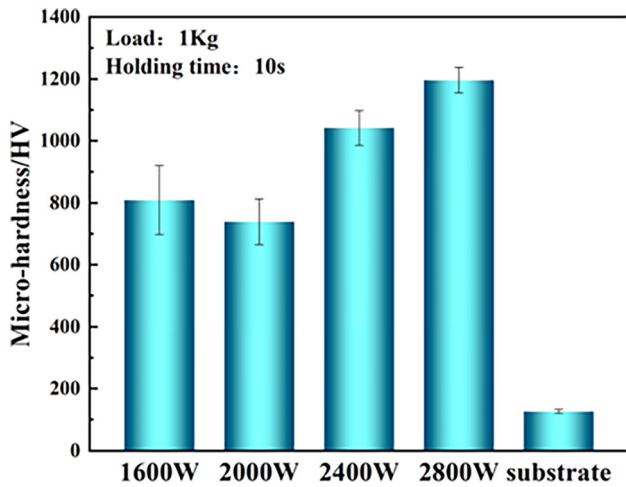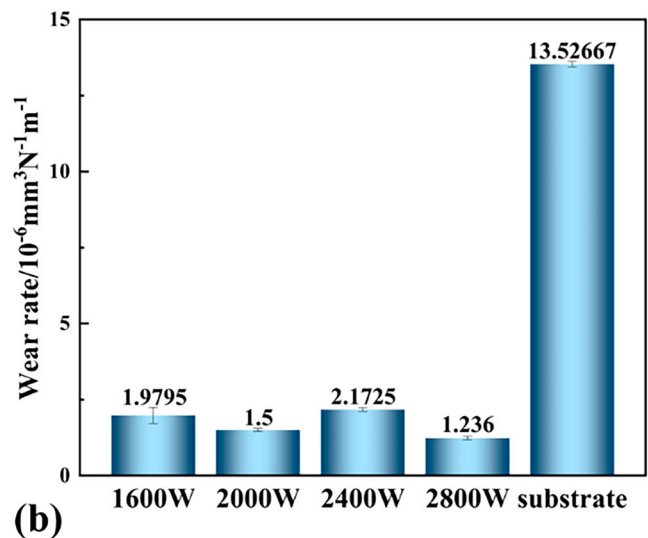

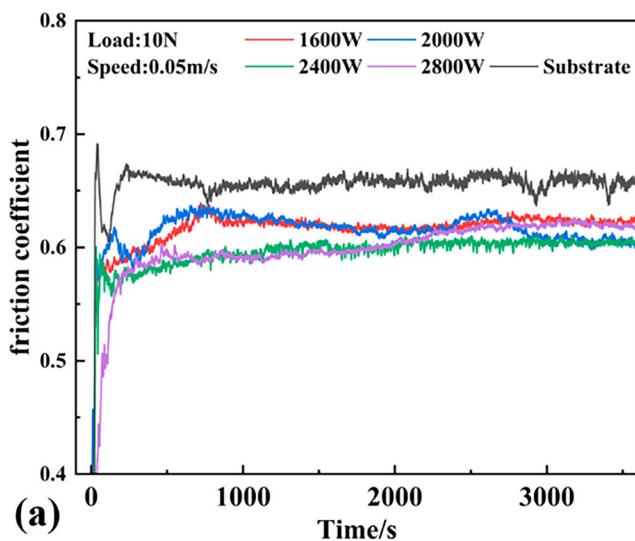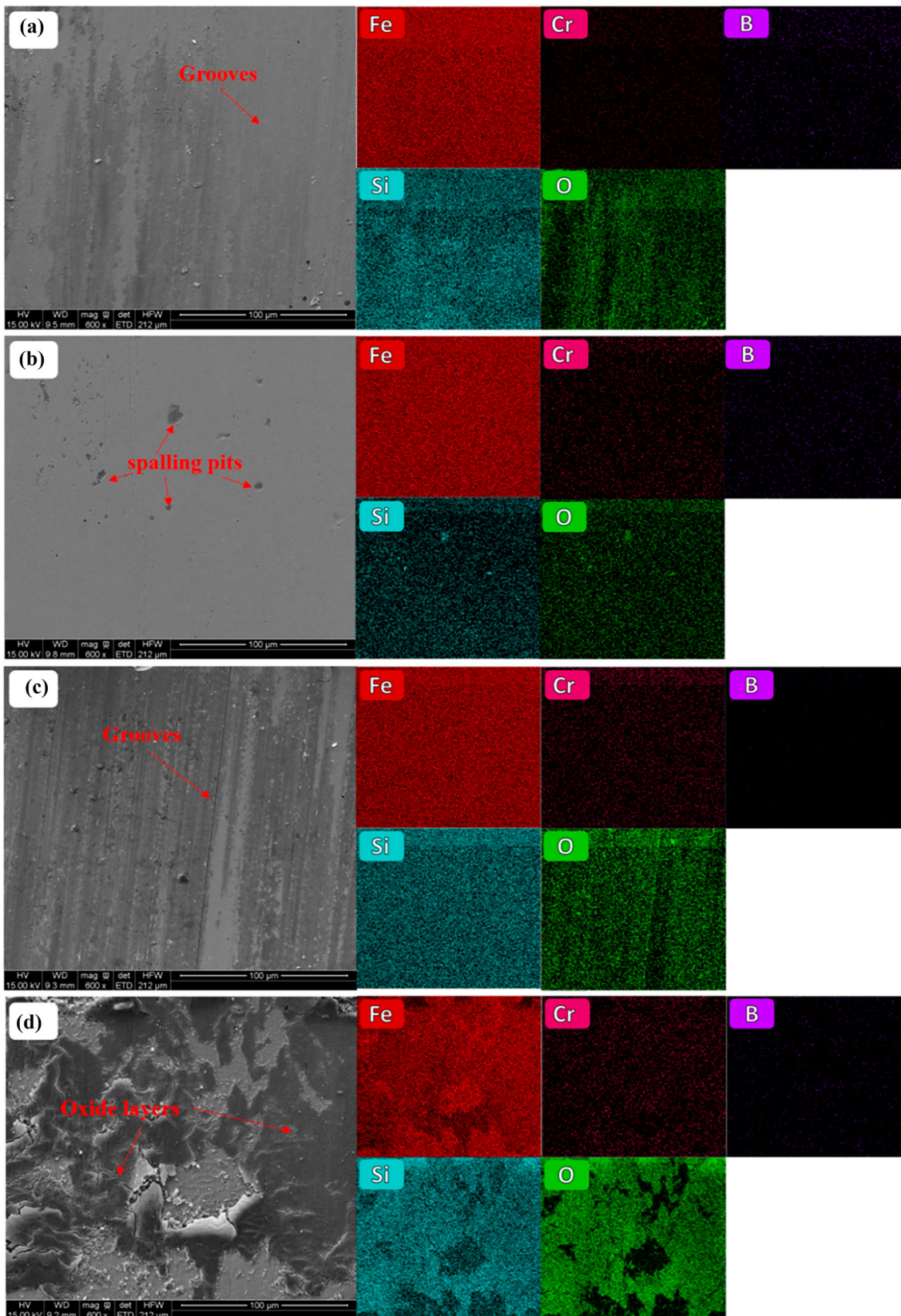**Fig. 7** Microhardness of coating and substrate

Fig. 8 Friction coefficient and wear rate of ultra-high-speed laser cladding coating

Fig. 9 SEM images of wear and corresponding EDS mapping: (a) 1600W, (b) 2000W, (c) 2400W, (d) 2800W

compound content. At the same time, some nanocrystals are generated inside the ultra-high-speed laser melting coating. They play the role of diffuse reinforcement inside the coating, hindering the internal dislocation movement and improving the microhardness of the coating. Therefore, under the synergistic effect of intermetallic compounds (IMC) and
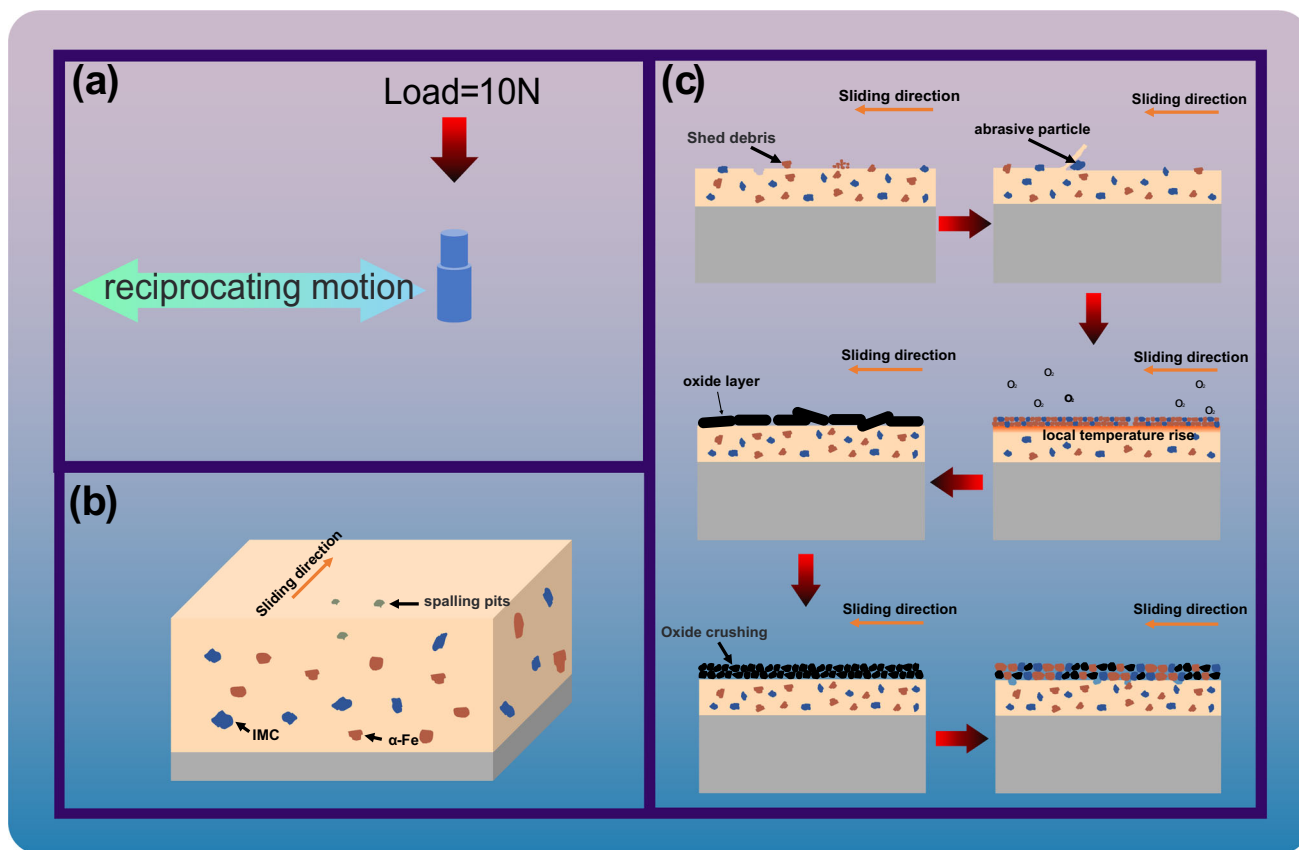
Fig. 10 Wear test of the coating of Fe-based amorphous alloy: (a) Friction diagram, (b) Coating surface wear diagram, (c) Wear mechanism diagram

nanocrystals, the microhardness of the coating is greatly improved.

Fig. 8(a) is the friction coefficient curve of the coating. The friction coefficients are 0.615, 0.614, 0.594, and 0.596, respectively, and the friction coefficient of the substrate is 0.654. When the power is 2400W and 2800W, the friction coefficient of the coating is the lowest, which is due to the lubricating effect of the oxide layer during the wear process (this will be proved in Fig. 10 below). Combined with Fig. 7 and 8(b), because the microhardness of all coatings is much larger than that of the substrate, the wear rate of the coatings is lower than that of the substrate. The wear rate of the coating with power of 2800W is the lowest, and the wear rate of the coating with power of 2400W is the highest. According to the Akkad wear theory, the wear rate should be inversely proportional to the microhardness. However, according to the above analysis, the wear resistance of the coating with a power of 2400W seems to be contrary to the theoretical law, indicating that microhardness is not the only factor affecting wear resistance of amorphous alloys. In addition, the toughness of the material may be a factor affecting the wear resistance of the material (Ref 28). It has been reported in the literature that, unlike metal alloys that exhibit strain hardening, amorphous alloys are brittle and wear resistance is often disproportionate to hardness (Ref 29, 30). According to Segu et al., after the amorphous phase in amorphous alloys is crystallized, the hardness and toughness of the material will increase, thus improving the wear resistance (Ref 31). Therefore, the wear resistance of 2000W coating is better than that of 1600W

coating. After excessive crystallization of the amorphous phase in the coating, the wear resistance will be reduced, so the wear resistance of the 2400W coating is greatly reduced. The results show that the amorphous phase helps to improve the wear resistance of the coating, and it can be inferred that the hardness and wear resistance of the coating will be greatly reduced when the amorphous phase in the coating is completely crystallized. When the laser power is 2800W, the wear resistance of the coating shows that the intermetallic compounds also have an important effect on the wear resistance of the material. Therefore, the balance of amorphous phase, crystalline phase, and intermetallic compound content helps to improve the wear resistance of the coating.

Shown in Fig. 9, the abrasion morphology and EDS energy spectra of the samples with different laser powers are displayed. Different wear mechanisms are shown with increasing laser power. At a laser power of 1600W, some shallow grooves, abrasive chips, punctate flaking pits, and gray phases appeared on the coating surface. According to the EDS result, the gray phase contained trace O elements and was characterized by slight oxidation. These phenomena indicate that the main wear mechanisms of the coating are slight abrasive wear, adhesive wear, and oxidative wear. It can be seen from Fig. 9(b) that when the laser power was 2000 W, the wear surface of the coating had more spalling pits and a small number of shallow grooves, indicating that the wear mechanism of the coating was slightly abrasive wear and severe adhesive wear. The microhardness of the coating was the lowest, while the toughness may be the best. Therefore, the wear resistance of the coating

will also be improved to a certain extent. Fig. 9(c) shows that when the laser power was 2400 W, a large number of deep grooves, wear debris, and oxide layers appeared on the wear surface of the coating, indicating that the wear mechanism of the coating was severe abrasive wear and oxidation wear. It can be seen from Fig. 9(d) that when the laser power was 2800W, the wear surface of the coating underwent a severe oxidation reaction, and a thicker oxide layer was formed. The main components of the oxide layer were silicon oxide and iron oxide. Therefore, severe oxidation wear was the wear mechanism of the coating.

According to the coating wear morphology and energy spectrum analysis results, the coating wear mechanism diagram (Fig. 10) was drawn to explain the coating wear mechanism in more detail. Fig. 10(b) is a schematic diagram based on Fig. 4, in which the IMC is an intermetallic compound embedded in a pale yellow amorphous structure with no obvious features. During the friction process, due to the action of the grinding ball, the surface of the coating has plastic deformation, resulting in some materials of the coating falling off. The softer α-Fe phase is coated on the surface of the coating under the action of the grinding ball, and the harder amorphous phase and intermetallic compound are broken into small particles under the action of the grinding ball and the coating. These abrasive particles form grooves on the surface of the coating by cutting. The amorphous phase and intermetallic compounds can effectively resist plastic deformation and reduce the wear rate of the coating due to their high hardness. In addition, molecular forces and frictional heat bind the coating surface to the ball contact zone. When the shear force exceeds the strength of the solder joint, it causes fracture and forms pitting pits. The strong friction between the coating and the grinding ball produces local high temperature, and the oxide layer formed by the contact of oxygen and the coating surface acts as support and lubrication. As the friction continues, the oxide layer is broken, and oxygen comes into contact with the coating surface again, forming a new oxide layer, which deepens the degree of oxidative wear. At the same time, the constantly broken oxide layer forms new abrasive particles, which further intensifies the abrasive wear effect on the coating. Therefore, during the wear process, due to the synergistic effect of oxidative wear and abrasive wear, the coating with a power of 2400 W has the most severe wear degree.

4. Conclusions

The coatings of Fe-based amorphous alloys with laser powers of 1600W, 2000W, 2400W, and 2800W were prepared by ultra-high-speed laser cladding technology. The microstructure and tribological properties of these coatings were investigated. The conclusions are summarized as follows:

(1) The 1600W and 2000W coatings consist of amorphous, α-Fe, Fe_3Si and Fe_2Si. 2400W and 2800W coatings consist of amorphous, α-Fe, Fe_3Si, Fe_2Si, $Fe_{23}B_6$, Fe_3B and Fe_2B.
(2) With the increase of power, the crystal morphology at the interface between the bottom of the coating and the substrate changes from cellular crystals to planar crystals and columnar dendrites. The amorphous phase decreases and the crystalline phase increases at the top of the coat-

ing. The amorphous and crystal phases are mixed more evenly.
(3) As the power increases, the amorphous phase content decreases, the intermetallic compounds increase, and the microhardness decreases first and then increases. When the laser power is 2800W, the hardness of the coating is the highest, which is because the synergistic effect of intermetallic compounds and amorphous compounds improves the hardness of the coating. At the same time, the decrease of the amorphous phase will increase the wear rate of the coating, and the content of the amorphous phase, crystalline phase, and intermetallic compound in the coating will decrease the wear rate when the content reaches a balance.

Data Availability

The raw/processed data required to reproduce these findings cannot be shared at this time as the data also forms part of an ongoing study.

Conflict of interest

The authors declare that they have no known competing financial interests or personal relationships that could have appeared to influence the work reported in this paper.

References

1. Y.Y. Zhu, Z.G. Li, R.F. Li, M. Li, X.L. Daze, K. Feng and Y.X. Wu, Microstructure and Property of Fe-Co-B-Si-C-Nb Amorphous Composite Coating Fabricated by Laser Cladding Process, *Appl. Surf. Sci.*, 2013, **280**, p 50–54.
2. C.L. Zhu, Q. Wang, Y.M. Wang, J.B. Qiang and C. Dong, Co-B-Si-ta Bulk Metallic Glasses Designed Using Cluster Line and Alloying, *J. Alloys Compd.*, 2010, **504**, p S34–S37.
3. C. Tan, H. Zhu, T. Kuang, J. Shi, H. Liu and Z. Liu, Laser Cladding Al-Based Amorphous Nanocrystalline Composite Coatings on AZ80 Magnesium Alloy Under Water Cooling Condition, *J. Alloys Compd.*, 2017, **690**, p 108–115.
4. R. Li, Y. Jin, Z. Li, Y. Zhu and M. Wu, Effect of the Remelting Scanning Speed on the Amorphous Forming Ability of Ni-Based Alloy Using Laser Cladding Plus a Laser Remelting Process, *Surf. Coat. Technol.*, 2014, **259**, p 725–731.
5. S.Y. Hong, W.H. Guo and H.W. Kui, Metastable Liquid Miscibility Gap in Pd-Si and Its Glass-Forming Ability: Part III, *J. Mater. Res.*, 1999, **14**, p 3668–3672.
6. T.M. Yue, Y.P. Su and H.O. Yang, Laser Cladding of Zr65Al7.5Ni10-Cu17.5 Amorphous Alloy on Magnesium, *Mater. Lett.*, 2007, **61**, p 209–212.
7. K.J. Huang, C.S. Xie and T.M. Yue, Microstructure of cu-Based Amorphous Composite Coatings on AZ91D Magnesium Alloy by Laser Cladding, *J. Mater. Sci. Technol.*, 2009, **25**, p 492–498.
8. N. Luo, C. Scheitler, N. Ciftci et al., Preparation of Fe-Co-B-Si-Nb Bulk Metallic Glasses by Laser Powder Bed Fusion: Microstructure and Properties, *Mater Charact*, 2020, **162**, 110206

9. Q. Zhu, S. Qu, X. Wang et al., Synthesis of Fe-Based Amorphous Composite Coatings with Low Purity Materials by Laser Cladding, *Appl. Surf. Sci.*, 2007, **253**(17), p 7060–7064.

10. H.X. Li, Z.C. Lu, S.L. Wang et al., Fe-Based Bulk Metallic Glasses: Glass Formation, Fabrication, Properties and Applications, *Prog. Mater. Sci.*, 2019, **103**, p 235–318.

11. Y. Lu, G. Huang, Y. Wang et al., Crack-Free Fe-Based Amorphous Coating Synthesized by Laser Cladding, *Mater. Lett.*, 2018, **210**, p 46–50.

12. C. Liu, S. Jen, J. Juang and C. Lo, Ferromagnetic Resonance Properties of Fe81- xNixGa19/Si (100) and Fe81-yNiyGa19/glass Films, *J. Alloys Compd.*, 2013, **562**, p 111–115.

13. S. Zhou, Y. Xu, B. Liao, Y. Sun, X. Dai, J. Yang and Z. Li, Effect of Laser Remelting on Microstructure and Properties of WC Reinforced Fe-Based Amorphous Composite Coatings by Laser Cladding, *Opt. Laser Technol.*, 2018, **103**, p 8–16.

14. S.L. Wang, Z.Y. Zhang, Y.B. Gong and G.M. Nie, Microstructures and Corrosion Resistance of Fe-Based Amorphous/Nanocrystalline Coating Fabricated by Laser Cladding, *J. Alloys Compd.*, 2017, **728**, p 1116–1123.

15. G. He and Q. Chen, Interpretation of Densification Behavior of Spark Plasma Sintered Fe-Based Metallic Glass Powders from the Standpoint of Internal Friction, *J. Alloy. Compd.*, 2019, **797**, p 213–221.

16. W. Yuan, R. Li, Z. Chen, J. Gu and Y. Tian, A Comparative Study on Microstructure and Properties of Traditional Laser Cladding and High-Speed Laser Cladding of Ni45 Alloy Coatings, *Surf. Coat. Technol.*, 2020, **405**, p 126582.

17. N. Jeyaprakash, C.-H. Yang and K. Ramkumar, Microstructure and Wear Resistance of Laser Cladded Inconel 625 and Colmonoy 6 Depositions on Inconel 625 Substrate, *Appl. Phys. A*, 2020, **126**, p 1–11.

18. W. Yuan, R. Li, Y. Zhu, Y. Zhao, X. Zhang, B. Liu and B. Zhang, Structure and Properties of Nickel-Plated CNTs/Fe-Based Amorphous Composite Coatings Fabricated by High-Speed Laser Cladding, *Surface Coatings Technol.*, 2022, **438**, p 128363.

19. K. Li, J. Liang and J. Zhou, Preparation and Characterization of Laser Cladded FeCrMoBSi Amorphous Composite Coatings, *Surf. Coat. Technol.*, 2021, **423**, 127520

20. M. Xiao, H. Gao, L. Sun, Z. Wang, G. Jiang, Q. Zhao, C. Guo, L. Li and F. Jiang, Microstructure and Mechanical Properties of Fe-Based Amorphous Alloy Coatings Prepared by Ultra-High Speed Laser Cladding, *Mater. Lett.*, 2021, **297**, p 130002.

21. C.-S. Chien, C.-W. Liu and T.-Y. Kuo, Effects of Laser Power Level on Microstructural Properties and Phase Composition of Laser-Clad Fluorapatite/Zirconia Composite Coatings on Ti6Al4V Substrates, *Materials*, 2016, **9**, p 380.

22. B. Manne, M.R. Srikanth Bontha, M.K. Ramesh and V.K. Balla, Solid State Amorphization of Mg-Zn-Ca System Via Mechanical Alloying and Characterization, *Adv. Powder Technol.*, 2017, **28**(1), p 223–229.

23. E. Rabinowicz, Influence of Surface Energy on Friction and Wear Phenomena, *J. Appl. Phys.*, 1961, **32**, p 1440–2000.

24. M.Z. Ibrahim, A.A.D. Sarhan, T.Y. Kuo et al., Developing a New Laser Cladded FeCrMoCB Metallic Glass Layer on Nickel-Free Stainless-Steel as a Potential Superior Wear-Resistant Coating for Joint Replacement Implants, *Surf. Coat. Technol.*, 2020, **392**, 125755

25. H.Z. Wang, Y.H. Cheng, X.C. Zhang et al., Effect of Laser Scanning Speed on Microstructure and Properties of Fe Based Amorphous/Nanocrystalline Cladding Coating, *Mater. Chem. Phys.*, 2020, **250**(7), 123091

26. K. Li, J. Liang and J. Zhou, Preparation and Characterization of Laser Cladded FeCrMoBSi Amorphous Composite Coatings, *Surface Coat. Technol.*, 2021, **423**, p 127520.

27. Q. Wang, X. Bai, B. Sun et al., Influence of Si on Tribological Behavior Of Laser Cladded Fe-Based Amorphous/Crystalline Composite Coatings, *Surf. Coat. Technol.*, 2021, **405**, 126570

28. Z. Wang, F. Chen, Y. Dong, Z. Cai, P. Zhang, J. Chen, G. Le and i Zeng, Effect of Heat-Treatment Time on Microstructure and Tribological Behavior of (TiVCrAlMo)N High-Entropy Alloy Films, *Surface Coat. Technol.*, 2022, **443**, p 128618.

29. M.L. Rahaman, L.C. Zhang and H.H. Ruan, Understanding the Friction and Wear Mechanisms of Bulk Metallic Glass Under Contact Sliding, *Wear*, 2013, **304**(1–2), p 43–48.

30. Z. Liao, N. Hua, W. Chen et al., Correlations Between the Wear Resistance and Properties of Bulk Metallic Glasses, *Intermetallics*, 2018, **93**, p 290–298.

31. D.Z. Segu, J.H. Choi, S. Yi et al., Dry Sliding Tribological Properties of Fe-Based Bulk Metallic Glass, *Tribol. Lett.*, 2012, **47**, p 131–138.